

Active cargo positioning in antiparallel transport networks

Mathieu Richard, Carles Blanch-Mercader, Hajer Ennomani, Wenxiang Cao, Enrique de La Cruz, Jean-François Joanny, Frank Jülicher, Laurent Blanchoin, Pascal Martin

▶ **To cite this version:**

Mathieu Richard, Carles Blanch-Mercader, Hajer Ennomani, Wenxiang Cao, Enrique de La Cruz, et al.. Active cargo positioning in antiparallel transport networks. Proceedings of the National Academy of Sciences of the United States of America, 2019, 116 (30), pp.14835-14842. 10.1073/pnas.1900416116 . hal-02185109

HAL Id: hal-02185109
https://hal.science/hal-02185109

Submitted on 22 Oct 2020

HAL is a multi-disciplinary open access archive for the deposit and dissemination of scientific research documents, whether they are published or not. The documents may come from teaching and research institutions in France or abroad, or from public or private research centers.

L'archive ouverte pluridisciplinaire **HAL**, est destinée au dépôt et à la diffusion de documents scientifiques de niveau recherche, publiés ou non, émanant des établissements d'enseignement et de recherche français ou étrangers, des laboratoires publics ou privés.

Active cargo positioning in antiparallel transport networks.

Mathieu Richard[1], Carles Blanch-Mercader[2], Hajer Ennomani[3], Wenxiang Cao[4], Enrique De La Cruz[4], Jean-Francois Joanny[1], Frank Jülicher[5], Laurent Blanchoin[6], Pascal Martin[1]

[1]Institut Curie, [2]University of Geneva, [3]Biosciences and Biotechnology Institute of Grenoble, [4]Yale University, [5]Max Planck Institute for the Physics of Complex Systems, [6]Interdisciplinary Research Institute of Grenoble (IRIG)

Submitted to Proceedings of the National Academy of Sciences of the United States of America

Cytoskeletal filaments assemble into dense parallel, antiparallel or disordered networks, providing a complex environment for active cargo transport and positioning by molecular motors. The interplay between the network architecture and intrinsic motor properties clearly affects transport properties but remains poorly understood. Here, by using surface micro-patterns of actin polymerization, we investigate stochastic transport properties of colloidal beads in antiparallel networks of overlapping actin filaments. We found that 200-nm beads coated with myosin-Va motors displayed directed movements towards positions where the net polarity of the actin network vanished, accumulating there. The bead distribution was dictated by the spatial profiles of local bead velocity and diffusion coefficient, indicating that a diffusion-drift process was at work. Remarkably, beads coated with heavy mero-myosin-II motors showed a similar behavior. However, although velocity gradients were steeper with myosin II, the much larger bead diffusion observed with this motor resulted in less precise positioning. Our observations are well described by a three-state model, in which active beads locally sense the net polarity of the network by frequently detaching from and reattaching to the filaments. A stochastic sequence of processive runs and diffusive searches results in a biased random walk. The precision of bead positioning is set by the gradient of net actin polarity in the network and by the run length of the cargo in an attached state. Our results unveiled physical rules for cargo transport and positioning in networks of mixed polarity.

myosin | actin cytoskeleton | intracellular transport | stochastic processes

Introduction

Controlling transport at microscopic scales poses a fundamental challenge in biology, engineering and physics. In the cell, molecular motors use cytoskeletal filaments as polar tracks for directed transport (1). However, the filaments are organized in dense networks with structural heterogeneities (2), which impart stringent physical constraints according to two basic mechanisms (3). First, disorder in filament orientations, as well as branching, results in intersections that can affect the directionality of cargo transport (4). Second, networks of mixed polarity foster bidirectional movements either because a given cargo can interact with multiple filaments simultaneously, resulting in a tug-of-war (5), or stochastically detach and reattach to a different filament (6, 7). Conversely, the outcome of motor-driven transport in a given cytoskeletal architecture also depends on the single-molecule properties of the motors (8-10) and on their collective organization (8, 11, 12).

Two types of theoretical approaches have been proposed to describe the collective behavior of motor assemblies attached to the same cargo. Microscopic theories aim at determining the collective behavior from single motor properties (13-16). Alternatively, coarse grained theories focus on global properties of cargo dynamics resulting from stochastic binding to and unbinding from cytoskeletal filaments (17). The latter approach introduces only a few effective parameters, such as binding and unbinding rates as well as transport velocity of the cargo, and does not rely on detailed knowledge on single motors. Thanks to its relative simplicity, the coarse-grained approach is well adapted for the study of cargo transport in complex environments (6, 7).

In this work, we developed an in-vitro assay to study the interplay between the cytoskeletal organization and motor properties for cargo transport. We monitored transport of beads that were actively propelled by either processive myosin-Va or non-processive heavy-mero myosin-II motors in antiparallel networks of actin filaments with exponential density profiles. We found that the myosin-coated beads were actively positioned to regions where the net polarity of the actin network vanished and with a higher precision than the characteristic length associated with polarity gradients of the network. A theoretical description of the transport process at the coarse-grained level was able to clarify the physical rules underlying active cargo trapping in antiparallel networks depending on motor properties and filament-polarity gradients.

Results

Antiparallel actin networks of controlled architecture. We designed surface micro-patterns of the nucleation-promoting factor pWA to control the geometry and collective organization of growing actin filaments (18, 19). Our patterns were composed of parallel nucleation lines spaced by a distance $L \approx 40$ μm. Actin filaments extended perpendicularly to the nucleation lines by monomer incorporation to their barbed ends; the pointed ends of

Significance

Cellular functions rely on small groups of molecular motors to transport their cargoes throughout the cell along polar filaments of the cytoskeleton. Cytoskeletal filaments self-assemble into dense networks comprising intersections and filaments of mixed polarity, challenging directed motor-based transport. Using micro-patterns of actin polymerization in-vitro, we investigated stochastic transport of colloidal beads in antiparallel networks of overlapping actin filaments. We found that beads coated with myosin motors sensed the net polarity of the actin network, resulting in active bead positioning to regions of neutral polarity with a precision depending on the motor type. A theoretical description of our experimental results provides the key physical rules for cargo transport and positioning in filament networks of mixed polarity.

Reserved for Publication Footnotes

submitted manuscript

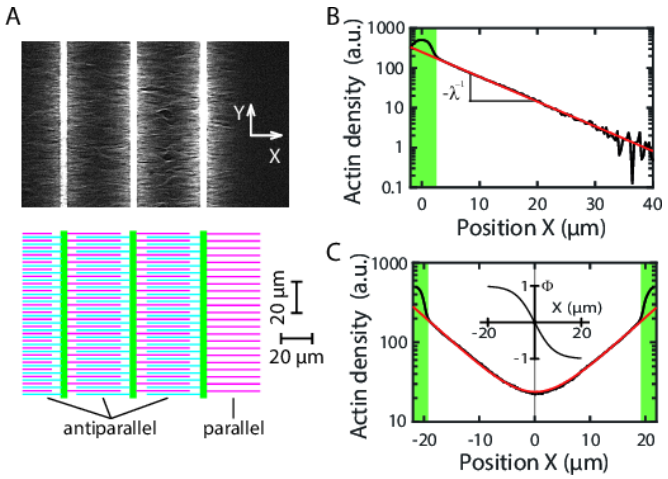


Fig. 1. Bi-dimensional network of antiparallel actin filaments in vitro. A: Fluorescence imaging (top) and schematic representation (bottom) of the actin architecture. Actin filaments grew from a surface pattern of parallel lines (green) coated with a nucleation-promoting-factor of actin polymerization. The filaments are oriented along axis X, thus perpendicular to the nucleation lines (axis Y), with their barbed ends located away from the lines. An antiparallel network of overlapping actin filaments was established between neighboring nucleation lines. The line at the right end of the pattern has no neighbor on its right-hand side and thus provides a parallel network of filaments. **B:** Actin density profile for the parallel network. This semilog plot shows that the profile is well described by an exponential function (red line). The inverse absolute slope of the curve corresponds to the mean length, here λ = 7 µm, of the actin filaments in the network. **C:** Actin density profile for the antiparallel network. The profile is well described (red line) by the sum of two mirror-symmetric exponential with the same characteristic length as that obtained in **B**. In **B** and **C**, the nucleation lines are marked by the green shaded areas. Inset: The net polarity of the antiparallel network is plotted as a function of position *X*, where λ represents the mean-actin length measured in **A**; the net polarity is null at the center of the network, where . Nucleation lines are spaced by 40 µm and have a width of 3 µm. The actin density profiles were measured after 30 min of polymerization.

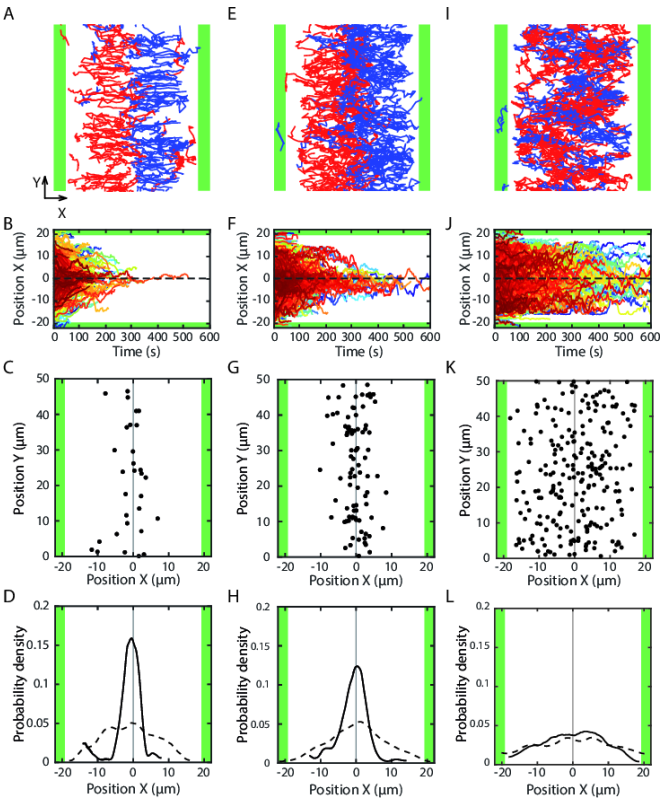


Fig. 2. Bead transport and steady-state distribution in antiparallel actin networks. Beads were coated with molecular motors (myosin Va in **A-D**; myosin II HMM in **E-H**) or passivated with BSA (**I-L**). **A, E** and **I**: Bead trajectories within the plane of the actin network. Red (blue): trajectories with a net positive (negative) movement along axis X. Motor coated beads (**A** and **E**) displayed a directed movement towards the midline of the pattern (X=0), where they accumulated. Instead, passive beads (**I**) showed a diffusive exploration between the two nucleation lines. **B, F** and **J**: Bead position along the axis (X) of the actin filaments as a function of time. Most beads take less than 200 s to reach the center of the network. **C, G** and **K**: Bead positions in the network 30 min after actin polymerization was initiated. Because they are too small (200-nm diameter) to be clearly visualized, the beads are here represented by 1.2-µm disks, corresponding to a fivefold increase from their actual size. **D, H** and **L**: Distribution of bead positions along axis X at steady state (solid line) and when the beads where first detected (dashed line). The nucleation lines are marked by the green shaded areas. The surface fraction of the network occupied by the beads was maximal at the center but remained smaller than $5{\cdot}10^{-4}$, corresponding at most to one bead every 60 µm^2. Because of data folding (see Methods) and bead-size magnification, the surface fraction occupied by the beads in panels **C, G** and **K** is 1,512-fold that measured in reality.

the filaments were localized on the pattern, whereas the barbed ends moved away from the nucleation zones. After ~10 min of polymerization, filaments growing in opposite directions from adjacent lines overlapped, yielding an anti-parallel network (Fig. 1). Inclusion of methylcellulose as a depleting agent ensured that most of the network remained within ~200 nm of the glass surface (20), thus forming an actin sheet.

We took advantage of the nucleation line at one edge of the pattern to characterize the architecture of a parallel actin network, without interference from actin filaments coming in opposite direction from a neighboring nucleation line. In this case, the actin density profile along an axis X perpendicular to the nucleation line followed an exponential decay $\rho(X) \propto \exp(-X/\lambda)$ (Fig. 1B). There, the decay length λ = 8.2±1.1 µm (n = 29) corresponds to the mean length of actin filaments in the network.

In between two parallel nucleation lines, the actin density profile of the anti-parallel network displayed mirror symmetry about the center, where the density was minimal. In the following, the center was set at $X = 0$. Corresponding to this symmetry, the profile $\rho(X) = \rho^+(X) + \rho^-(X)$ was described by the sum of two mirror-symmetric exponentials $\rho^\pm(X) = (\rho_0/2)\exp(\mp X/\lambda)$; equivalently $\rho(X) = \rho_0 \cosh(X/\lambda)$ with ρ_0 the total actin density at the center (Fig. 1C). The mean filament length λ was indistinguishable from that measured with a single line at the edge of the pattern. We define the net polarity of the actin network as $\Phi(X) = (\rho^+(X) - \rho^-(X))/(\rho^+(X) + \rho^-(X)) = \tanh(X/\lambda)$ (Fig. 1C, inset). At the center of the actin density profile, the net polarity vanished ($\Phi(0) = 0$) and the net-polarity gradient was given by the inverse of the mean actin length ($\Phi'(0) = 1/\lambda$). Thus, the shorter the average length of the filaments, the steeper the gradient of net polarity. Because the pattern spacing was significantly larger than the mean filament length ($L \gg \lambda$), all filaments had nearly the same polarity near each of the nucleation lines ($\Phi(\pm L/2) = \mp 1$).

Active centering of myosin-coated beads. We tracked the trajectories of 200-nm beads that were coated with either myosin Va or heavy-mero myosin II (hereafter called 'myosin V' or 'myosin II' for simplicity) after they landed on the actin network by sedimentation from the bulk. Both types of myosin-coated beads showed directed trajectories towards the midline of the network, hereafter called the center (Fig. 2A-B and E-F). Remarkably, although there were enough long filaments in the network to guide myosin-based transport all the way to the other side of the pattern (SI Appendix, Fig. S1), the beads appeared unable to move a significant distance past the center, where the net polarity of the actin network vanished, accumulating there (Fig. 2C and

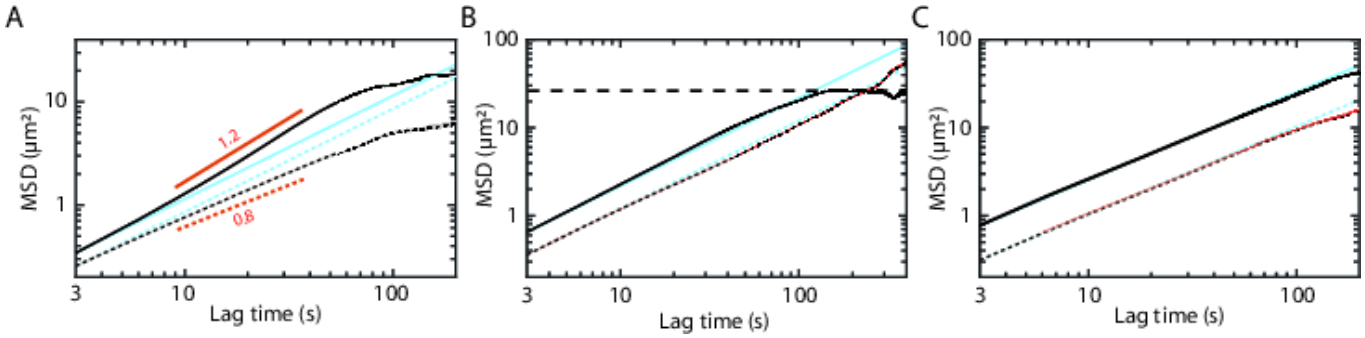


Fig. 3. Global analysis of bead transport. The mean squared displacement (MSD) along the X-axis (i.e. parallel to the actin filaments; solid black lines) and along the Y-axis (i.e. perpendicular to the actin filaments; dotted black lines) is plotted as a function of the lag time () for myosin-V-coated beads (**A**), for myosin-II-coated beads (**B**), and for BSA-coated beads (**C**). In all cases but for myosin-V coated beads, the relation is well described by for 100 s, corresponding to a diffusive one-dimensional transport with a diffusion coefficient . Fits to the data (cyan) yield: 0.062±0.004 μm^2/s (10 s) and 0.036±0.002 μm^2/s (n = 205) for myosin-V coated beads, 0.119±0.001 μm^2/s and 0.054±0.001 μm^2/s (n= 973) for myosin-II coated beads, and 0.129±0.002 μm^2/s and 0.052±0.001 μm^2/s (n = 538) for BSA-coated beads. At long times (100 s), the mean squared displacement of myosin-II coated beads along the X-axis saturates (dashed line), revealing confinement, but not along the Y-axis. Along the X-axis, the relation for myosin-V coated beads superlinear for 50 s, corresponding to persistent diffusion with (power-law fit for 50 s with R^2 = 0.9998; [1.21, 1.25], 95% confidence bounds; red solid line), and shows signs of saturation at larger lag times. This behavior is associated with sub-diffusion along the Y-axis according to (power-law fit for 80 s with R^2 = 0.9991; [0.79, 0.82], 95% confidence bounds; red dotted line). For each value of the lag time, the MSD was first time-averaged along each bead trajectory of longer duration than and then ensemble-averaged over all the trajectories that were detected.

Submission PDF

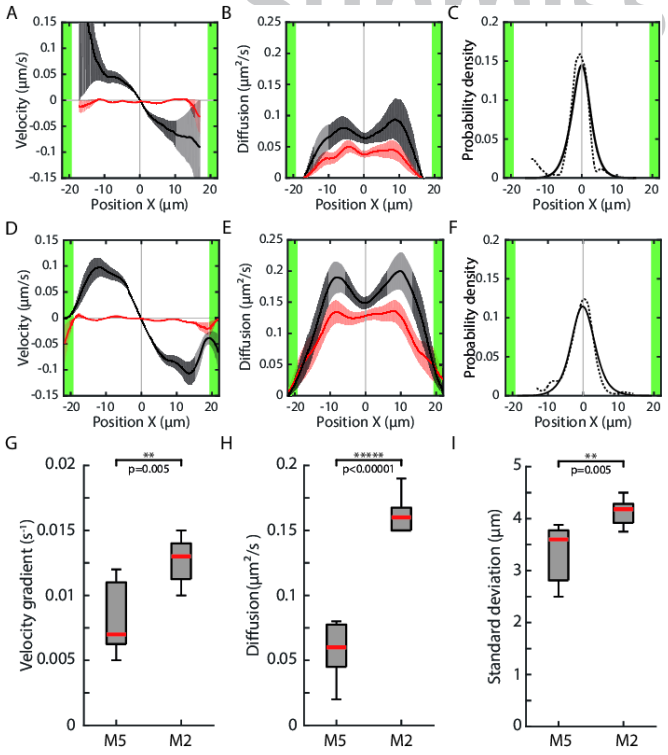


Fig. 4. Local analysis of active bead transport: velocity and diffusion-coefficient profiles. For myosin-V-coated beads (**A-C**) and myosin-II-coated beads (**D-F**), we plot the velocity (**A** and **D**) and diffusion coefficient (**B** and **E**) as a function of position *X* along the axis of the actin filaments (black lines: along X axis; red lines: along Y axis), as well as the steady-state distributions of bead positions (**C** and **F**) that were measured directly (dashed lines; same data as Fig. 2D and H) and predicted by a diffusion-drift process (solid lines; see Methods). In **G-I**, we show box plots of velocity gradient at the center (**G**), of the diffusion coefficient at the center (**H**) and of the standard deviation of bead position (**I**) for the two types of motor-coated-beads. The data shown in **G-I** results from N = 7 experiments in which myosin-V-coated beads and myosin-II-coated beads moved in the same antiparallel actin network, allowing for a direct comparison of their transport properties; statistical significance (stars) was assayed by paired-sample t-tests with p-values indicated on the figure.

G). As a result, the steady-state distribution of bead positions was peaked, in contrast to the flat distribution of initial bead positions corresponding to the first detection of the beads in the network (Fig. 2D and H). We considered that beads had reached steady state when their trajectories lasted at least 200 s (Fig. 2B and F; see Methods). On average, active cargo transport by myosin V or myosin II positioned the beads precisely at the center of the antiparallel actin network.

As a control, we also studied transport of beads passivated with BSA (Fig. 2I-L). These beads displayed a diffusive exploration of the space between nucleation lines, with trajectories that could start near a nucleation line and later explore regions near the opposite nucleation line (Fig. 2I and J), travelling long distances across the midline of the pattern. Accordingly, the distribution of bead positions at steady state was nearly flat (Fig. 2K and L). We note that passive interactions with the actin network or the substrate nevertheless resulted in a small centering effect, as the steady state distribution was slightly, but significantly, more peaked than the distribution of initial positions (compare dashed and solid lines in Fig. 2L).

Ensemble analysis of bead transport. To characterize bead transport, we computed the time- and ensemble-averaged squared displacement of the beads—the mean squared displacement$\mathrm{MSD}(\tau)$—as a function of the lag time τ. We recall that $\mathrm{MSD}(\tau) = 2D\,\tau$ for a purely diffusive one-dimensional transport characterized by a diffusion coefficient D, whereas a purely convective transport of velocity V should obey $\mathrm{MSD}(\tau) = V^2\,\tau^2$. In the case of beads coated with myosin V, motion analysis along the axis of the actin filaments (axis X; Fig. 1A) revealed that the relation $\mathrm{MSD}(\tau)$ was intermediate between those expected for pure diffusion and convective transport, corresponding to persisting diffusion with $\mathrm{MSD}(\tau) \propto \tau^{1.2}$ (τ <50 s; Fig. 3A). This behavior betrayed directed movements driven by myosin-V activity towards the midline of the pattern (Fig. 2A-B). Along the perpendicular axis (axis Y; Fig. 1A), the mean squared displacement was smaller and displayed a sub-diffusive behavior $\mathrm{MSD}(\tau) \propto \tau^{0.8}$ (τ <80 s; Fig. 3A).

In contrast, with beads coated with myosin II and for lag times τ< 100s, we observed that the bead ensemble had a transport behavior dominated by free diffusion (Fig. 3B). The diffusion coefficient was about 2.5 larger along the X-axis than along the Y-axis, reflecting the interaction of the beads with the anisotropic actin network. Beads near the nucleation lines displayed clear

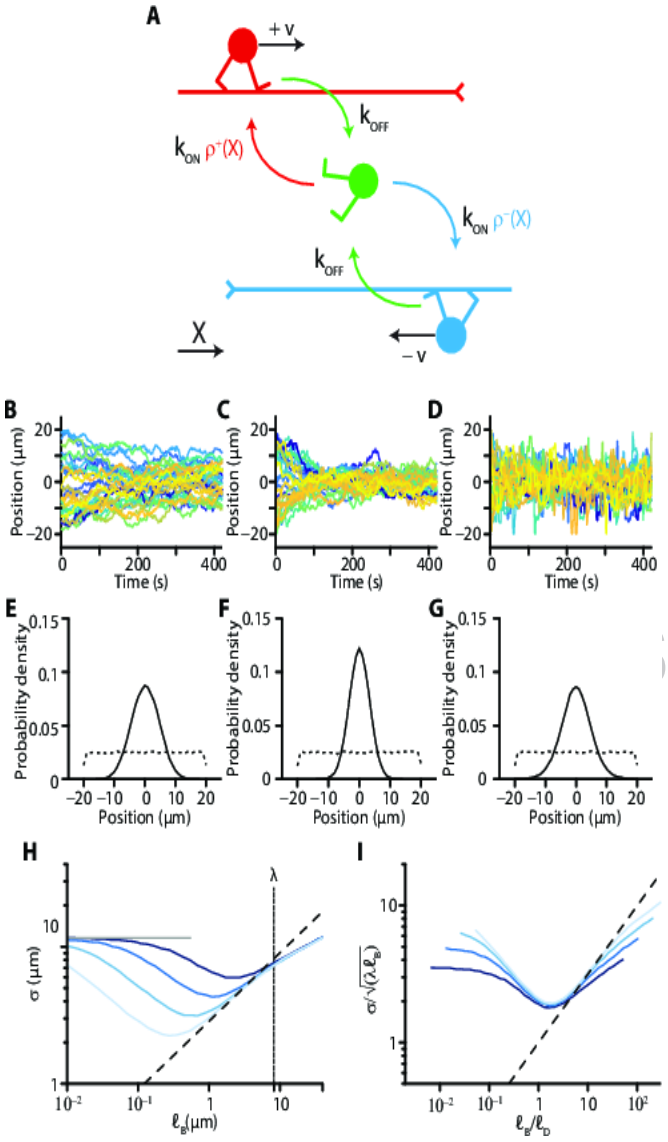


Fig. 5. Active positioning in a 3-state model of bead transport. A: Model myosin-coated beads can be attached to actin filaments and moving towards their barbed ends at velocity (red; state 1) or (blue; state 2) or detached and freely diffusing with a diffusion coefficient (green; state 3). Attached beads detach at a rate that does not depend on position in the network nor on filament polarity. Detached beads at position can attach to filaments of a given polarity (or) at rates proportional to the local density of the filaments, where corresponds to the mean filament length. **B-D:** Model-bead trajectories at low (0.5 μm/s and ; **B**), intermediate (2 μm/s and ; **C**)and high **(** 8 μm/s and ; **D**)velocity, which corresponds to increasing values of the ratio . Other parameter values in SI Appendix, Table S2 (Case 1). **E-G:** Model-bead distribution at the start of the simulation (dotted line) and at steady state (solid line) corresponding to the simulated trajectories shown in **B-D**, respectively. **H:** Standard deviation of bead position at steady state as a function of the ballistic length for four different values (0.3, 0.6, 1.1, and 2.2 μm, from light to dark blue) of the diffusion length at the center () of the filament network. The ballistic length was varied by changing the value of ; the diffusion length was varied by changing the value of ; other parameters in SI Appendix, Table S2 (Case 1). **I:** Same data as in **H**, but using normalized coordinates. In **H-I**, the dashed line corresponds to the relation .; in **H**, the horizontal grey solid line corresponds to the value expected for free one-dimensional diffusion in a box of size 40 μm.

directed movements towards the center of the pattern (Fig. 2E and F), as also observed with myosin V. However, although there were signs of persistent diffusion along the X-axis and of sub-diffusion along the Y-axis, as observed with myosin-V-coated beads, the signatures of directed movements were weak in our ensemble analysis of myosin-II-coated beads. At long times ($\tau >$ 100s), the mean squared displacement along the X-axis clearly saturated to a constant value: the beads were effectively trapped; confinement was not observed along the Y-axis, resulting in larger mean squared displacements along this axis than along the X-axis. With beads passivated by BSA, the mean squared displacement displayed anisotropic diffusion resembling that observed with myosin-II-coated beads, but with the important difference that no confinement was observed at long times for passive beads (Fig. 3C). In return, the saturation of the mean squared displacement that we observed with myosin-II-coated beads betrayed the activity of the motors, which strived to maintain the beads near the center of the network.

Spatial diffusion and drift profiles. Because the density and net polarity of the actin network varied with position along the X-axis, the transport properties of the beads were expected to be inhomogeneous. Spatial heterogeneities were averaged in the calculation of the mean-squared displacements (Fig. 3), which corresponded to ensemble averages of bead displacements, irrespective of their position in the network. To reveal the effects of the actin architecture on transport, we determined the local diffusion coefficient $D(X)$ and drift velocity $V(X)$ of the beads as a function of position X (Methods; Fig. 4). We observed that the drift velocity of the beads varied like the net polarity of the network (Fig. 1C, inset): the bead velocity saturated to a maximal (absolute) value near the nucleation line and declined (in absolute value) as the beads approached the center, changing sign there (Fig. 4A and D). In addition, the local diffusion coefficient displayed a local minimum near the center, where there was less actin (Fig. 4B and E).

Remarkably, the measured steady-state distributions of bead position (dashed lines in Fig. 4C and F) was well described by that predicted from a diffusion-drift process (P_{DD}) with the measured velocity and diffusion profiles (solid lines in Fig. 4C and F). In a diffusion-drift process, a convective flux $J_C = P_{DD}V$ transporting the beads towards the center of the network competes with a diffusive flux $J_D = -D\, dP_{DD}/dX$ that homogenizes the bead distribution. At steady state, because there is no apparent collective directional movement, the total flux $J_C + J_D = 0$, which yields $P_{DD}(X) = P_0 \exp\left(\int_0^X V(u)/D(u)\ du\right)$. Because $V(X)$ is odd and $D(X)$ is even, the distribution $P_{DD}(X)$ shows a peak at $X = 0$. The variance of bead position associated with a Gaussian approximation to the peak is given by $\sigma_{DD}^2 \cong D(0)/V'(0)$, where the prime corresponds to a spatial derivative. Thus, the steeper the velocity gradient and the lower the diffusion, the narrower the distribution. Notably, as the result of their larger speeds, myosin-II-coated beads displayed steeper gradients $V'(0)$ than myosin-V-coated beads (Fig. 4G). However, diffusion coefficients $D(0)$ were also much larger with myosin II than with myosin V (Fig. 4H). The standard deviation $\sigma$of bead position characterized the precision of bead positioning. We found$\sigma_{MV} = 3.3 \pm 0.6$ μm with myosin V and $\sigma_{MII} = 4.1 \pm 0.3$ μm with myosin II (mean±SEM; n = 7 experiments; Fig. 4I). Thus, active bead positioning at the center of the network was more precise with myosin V, by 25%. Note that these standard deviations are significantly smaller, by a factor two or more, than the characteristic length λ of the net-polarity gradient. Thus, bead positioning by motors was more precise than the lengthscale that characterizes structural heterogeneities of the actin network.

3-state model of bead transport. To understand the physical origin of active bead positioning in antiparallel filament networks, we worked within the framework of a 3-state model (6). A bead could be in one of the following three states (Fig. 5A): (state 1) attached to a filament oriented in the positive direction and moving along this filament at velocity $+v$, (state 2) attached to a filament oriented in the negative direction and moving along

Table 1. parameter values.

Parameter	Definition	Value for myosin V (mean±SEM; n = 11)	Value for myosin II (mean±SEM; n = 16)	Relation to other parameters
$\partial_X v_{EFF}(0)$ (s^{-1})	Measured velocity gradient at $X=0$	$(8.4 \pm 2.5)\cdot 10^{-3}$	$(12 \pm 2)\cdot 10^{-3}$	
$D_{EFF}(0)$ ($\mu m^2/s$)	Measured diffusion coefficient at $X=0$	0.06 ± 0.02	0.13 ± 0.04	
$\alpha = \tau_{ON}/\tau_{OFF}$	Ratio of mean durations in bound and unbound states	0.17 ± 0.02	0.05 ± 0.04	$\alpha = \frac{1}{\frac{v}{\lambda\, \partial_x v_{EFF}(0)} - 1}$
k_{OFF} (s^{-1})	Detachment rate from actin filaments	0.6 ± 0.3	1.6 ± 0.6	$k_{OFF} = \frac{v^2}{D_{EFF}(0)} \frac{\alpha}{\alpha+1}$
$k_{ON}\,\rho(0)$ (s^{-1})	Attachment rate to actin filaments	0.1 ± 0.07	0.08 ± 0.04	$k_{ON}\rho(0) = \frac{v^2}{D_{EFF}(0)} \frac{\alpha^2}{\alpha+1}$
ℓ_B (μm)	Ballistic length	0.77 ± 0.39	1.25 ± 0.47	$\ell_B = v/k_{OFF} = \frac{D_{EFF}(0)}{\lambda\, \partial_x v_{EFF}(0)}$

The first two rows show measured values of the velocity gradient and of the diffusion coefficient of myosin-coated beads at the center ($X = 0$) of antiparallel actin networks of the network (same data as in Fig. 4G-H). The last four rows show parameter values inferred from our theoretical description of bead transport using the relations shown on the last column with the intrinsic motor velocity $v = 0.46$ μm/s and 2 μm/s for myosin V and myosin II, respectively. We assumed here a vanishing diffusion length ($\ell_D \ll \ell_B$ or $D_\phi = 0$).

Submission PDF

this filament at velocity $-v$, or (state 3) detached and freely diffusing with a diffusion coefficient D_ϕ. We considered a uniform detachment rate constant k_{OFF} from the attached states 1 and 2 to the detached state 3. In contrast, attachment rate constants depended on the local density $\rho^{\pm}(X)$ of filaments of any given polarity: $k_{3\to1}(X) = k_{ON}\,\rho^{+}(X)$ and $k_{3\to2}(X) = k_{ON}\,\rho^{-}(X)$. Thus in the model, beads are more likely to attach to a filament of a given polarity when the corresponding filament density is larger than the density of filaments with the opposite polarity; this ingredient is key, because it provides a mechanism for sensing the net polarity of the network. Within this framework, we define two characteristic timescales: the mean time $\tau_{ON} = 1/k_{OFF}$ spent in an attached state (state 1 or 2) and the mean time $\tau_{OFF} = 1/(k_{ON}\,\rho_0)$ spent in the detached state (state 3), were $\rho_0 = \rho^{+}(0) + \rho^{-}(0)$ is the total actin density at the center ($X = 0$) of the network. Note that the mean time spent in the detached state depends on the total actin concentration and thus on position in the network; we use here as a reference the value of this characteristic time at the center, τ_{OFF}. We also define two characteristic lengthscales: the mean distance $\ell_B = v\tau_{ON}$ by which a bead travels along a filament in an attached state—the *ballistic length*—and the distance $\ell_D = \sqrt{D_\phi\,\tau_{OFF}}$ that controls the mean-squared displacement of a bead in the detached state as a result of Brownian motion—the *diffusion length*. In practice, we used exponential density profiles $\rho^{\pm}(X) = (\rho_0/2)\,\exp(\mp X/\lambda)$, as observed in experiments (Fig. 1C).

We simulated the stochastic dynamics of beads—called 'model beads' in the following (SI Appendix); at the start of the simulations, the model beads were randomly distributed in the antiparallel network. With two lengthscales and two timescales, we could operate in four distinct regimes of motion (SI Appendix, Fig. S3). In the regime of high attachment rates ($\tau_{ON} \gg \tau_{OFF}$), model beads are expected to move at velocity $\pm v$ near the edges of the antiparallel network, where $|X| \cong L/2 \gg \lambda$ and the net polarity $\Phi(X) \cong \pm 1$. However, the ensemble-averaged bead velocities that were measured at these positions in the antiparallel network (Fig. 4A and D) or at all positions in parallel networks (SI Appendix, Fig. S1) were almost one order of magnitude smaller than the natural velocity of the motors, as estimated in standard gliding assays (1). To account for this observation, we had to ensure in our simulations that the attachment probability of a bead was low, on the order of 10%, and thus choose $\tau_{ON} \ll \tau_{OFF}$. With this choice, we were able to reproduce (Fig. 5C) the active funneling observed with myosin-coated beads (Fig. 2B and F) when the model beads in our simulations traveled comparable distances in the attached and detached states ($\ell_B \sim \ell_D$). In this regime, the steady-state distribution of the model beads was peaked at the center of the network (Fig. 5C and F). Strikingly, by continuously increasing ℓ_B while keeping ℓ_D at a fixed value, we found that the standard deviation of model-bead position at steady state first decreased and reached a minimum at $\ell_B \cong 1.65\,\ell_D$, corresponding to an optimum of centering precision (Fig. 5H-I), before increasing again.

A hierarchy of lengthscales emerged naturally in the model: $L > \lambda > \ell_B \sim \ell_D$. The mean-actin length λ, which sets the lengthscale of the net-polarity gradient of the antiparallel network, had to be smaller than the size L of the network to ensure that the network was structurally inhomogeneous. Importantly, the condition $\lambda > \ell_B$ ensured that the bead trajectories in the attached state were short enough to sample the net-polarity gradient from detachment-reattachment events. Finally, centering required that the beads did not diffuse too far in the detached state ($\ell_B \sim \ell_D$; Fig. 5 and SI Appendix, Fig. S4) in order to keep a directionality of motion towards the center.

Provided that the density of the network varies slowly with position ($\lambda \gg \ell_B, \ell_D$), we could calculate analytically an effective drift velocity $V_{EFF}(X)$ and an effective diffusion coefficient $D_{EFF}(X)$ for the model beads (SI Appendix, section 3). In the experimentally-relevant limit of frequent detachment ($\alpha = \tau_{ON}/\tau_{OFF} \ll 1$), we found $V_{EFF}(X) \cong -v\,\alpha\,\sinh(X/\lambda)$ and $D_{EFF}(X) \cong D_\phi + (\ell_B^2/\tau_{ON})\,\alpha\,\cosh(X/\lambda)$. Notably, over a broad range of parameter values ($0.1 < \ell_B/\ell_D < 10$; SI Appendix, Fig. S6), the steady-state distribution of model-bead position was well approximated by that given by a diffusion-drift process using these velocity and diffusion profiles: $P_{th}(X) \cong P_0\,\exp\left\{\int_0^X [V_{EFF}(x)/\,D_{EFF}(x)]\,dx\right\}$. As in experiments, this distribution peaked in the center ($X = 0$): the active transport process brought the beads, on average, to the position where the net polarity of the network vanishes. Using a Gaussian approximation of the peak (SI Appendix, Eq S13), we estimate the variance of model-bead position

$$\sigma_{th}^2 \cong \ell_B(1 + (\ell_D/\ell_B)^2)/\Phi'(0)$$

where the polarity gradient at the center $\Phi'(0) = 1/\lambda$ is given by the mean filament length. In qualitative agreement with numerical estimates (Fig. 5H-I), the relation between the variance $\sigma^2_{\rm th}$ and the ballistic length ℓ_B (Eq. 1) shows a minimum; the minimal variance occurs here at $\ell_B = \ell_D$, where $\sigma^2_{\rm th}(\ell_B = \ell_D) = 2\ell_B/\Phi'(0)$. Clearly, at fixed ℓ_B, $\sigma^2_{\rm th}$ is minimal at $\ell_D = 0$.

By fitting the theory to our experiments, we were able to get numerical values for the parameters in the model. The actual value ℓ_D/ℓ_B is uncertain but our theory indicates that this ratio must display an upper bound ($\sim$4 for myosin V, $\sim$1.5 for myosin II; see SI Appendix, section 3) to account for the observed minimum of the effective diffusion coefficient at the center of the network (Fig. 4B and E; SI Appendix Fig. S5D). In the limit of small ℓ_D, parameter values are listed in Table 1. In particular, we inferred the ballistic length $\ell_B = \sigma^2/\lambda$ from the measured values of the variance σ of bead position (Fig. 4I) and of the mean actin length λ (Fig. 1B). We found $\ell_B = 0.77 \pm 0.39$ μm (n = 11) for myosin V that was smaller than the value $\ell_B = 1.25 \pm 0.47$ μm (n = 16) for myosin II, as required by Equation 1 (with $\ell_D/\ell_B \cong 0$) to ensure that bead positioning in a given actin network was more precise for with myosin V (Fig. 4). Near the optimal precision of positioning ($\ell_D/\ell_B \cong 1$), the ballistic length is half the value estimated when passive diffusion is ignored ($\ell_D/\ell_B \cong 0$).

Irrespective of the actual value of ℓ_D/ℓ_B, the model predicts that the precision of bead positioning (Eq. 1) should not depend on the size (L) of the actin network. This prediction was actually confirmed experimentally (SI Appendix, Fig. S2A). In addition, the standard deviation σ of bead position is expected to depend on the total actin density ρ_0 at the center, as can be seen by rewriting Equation 1 as $\sigma^2_{\rm th} \cong \lambda\ell_B\,(1 + \rho_c/\rho_0)$, in which $\rho_c = D_\emptyset/(\ell_B^2 k_{ON}) = \rho_0\,(\ell_D/\ell_B)^2$ corresponds to the critical actin density at which $\ell_D = \ell_B$. In the regime where the actin density is low enough ($\rho_0 \ll \rho_c$), the variance of bead position ought to be inversely proportional to the actin density ρ_0. Conversely at high actin densities ($\rho_0 \geq \rho_c$), the positioning precision should only weakly depend on the total actin density ρ_0. Increasing the concentration of monomeric actin in the polymerization mix from 2 μM to 5 μM had no significant effect on the measured value of σ (SI Appendix, Fig. S2B), suggesting that the condition $\rho_0 \geq \rho_c$ was satisfied and therefore that $\ell_B \geq \ell_D$ in our experiments.

Discussion

In this paper, we have presented a minimal in-vitro assay to study active cargo transport in mixed-polarity networks of cytoskeletal filaments. Focusing on the acto-myosin system, we found that myosin-coated beads can sense the net polarity of the network, which provides a cue for directed movements. Accordingly, the velocity of bead motion varied with the net actin polarity and went to zero at positions where the polarity vanished (Inset of Fig. 1C, Fig. 4A and D). As a result, the beads were actively trapped at these positions, providing a general mechanism of cargo positioning in mixed-polarity networks that does not depend on specific molecular recognition between a cargo and its target (21).

At steady state, the myosin-coated beads were confined within a region (Fig. 4) that was significantly smaller than the characteristic lengthscale associated with the net-polarity gradient of the antiparallel network, which was here set by the mean actin length λ (Fig. 1). Theoretical analysis via a coarse-grained model revealed that positioning depends not only on the steepness of the net-polarity gradient, but also on an interplay between the ballistic length ℓ_B and the diffusive length ℓ_D of the myosin-coated beads (Eq. 1). The ballistic length corresponds to the mean length that the myosin-coated beads travel in an attached state to actin before detaching and in turn probe the net polarity of the network. As long as $\ell_B > \ell_D$, the shorter the ballistic length, the finer the sampling of the net-polarity profile of the network, and thus the more precise the positioning (Fig. 5). However, the ballistic length cannot be too short for precise positioning: diffusive transport becomes limiting when $\ell_B < \ell_D$. Our model suggests that precise positioning emerges because the ballistic length ℓ_B ($\sim 1\mu m$) is shorter than the mean-actin length λ ($\sim 8\ \mu m$). Within our theoretical framework, active transport is described as a stochastic sequence of processive runs and diffusive searches that results in biased random walk towards a direction dictated by the net-polarity gradient.

An even simpler theoretical approach had been previously developed to describe dynein-driven transport in the mixed-polarity network of microtubules found in dendrites (7). However, this earlier work ignored diffusion in a detached state of the cargo and thus cannot describe the condition for optimal bead positioning that we reveal here (Fig. 5H-I). Our description extends a theory developed originally to capture endosomal transport during the asymmetric division of sensory organ precursors in Drosophila (6); we here consider slowly varying density profiles of antiparallel filament networks instead of overlapping homogeneous networks of opposite polarities.

Excluded-volume interactions between motor particles can lead to traffic jams, which shape the particle distribution at steady state (22). However, in our experiments, the surface fraction of the network occupied by the myosin-coated beads was so low (e.g. $\sim 10^{-4}$ for the myosin-II coated beads shown in Fig. 2G) that we could safely neglect steric bead interactions. Unidirectional transport has also been extensively studied in the context of cylindrical organelles such as filopodia or stereocilia. There, predicted motor distributions are critically controlled by boundary conditions, due to the influx of motors at the open end of the half-closed tube describing the geometry of those systems (23-25). In our experiments, beads instead enter the network by sedimentation from the bulk, in a direction perpendicular to the actin sheet. The sedimentation flux is uniform and very small (e.g. 0.025 bead/sec distributed over an area 40 μm × 350 μm of the actin network in the experiment corresponding to data shown in Fig. 2F, G and H). In addition, the width of the experimental bead distribution is one order of magnitude smaller than the width of the actin network (L = 40μm) and is vanishingly small at the boundaries (nucleation lines; Fig. 2). Thus at the edges, the bead influx along the axis of the filaments must be small.

Myosin-coated beads could in principle interact with multiple filaments of mixed polarity, resulting in a tug-of-war (26, 27). However, a tug-of-war is inherently unstable, resulting in bi-directional movements and bead switching between filaments (5, 13). Although we did not explicitly account for bead interaction with multiple filaments in our description of transport (SI Appendix), we observed that positioning was more precise in our simulations (SI Appendix, Fig. S7) when the beads were allowed to switch directly between the two attached states (States 1 and 2; Fig. 5A). In this case, analytical calculations in the small-diffusion limit ($L > \lambda > \ell_B \gg \ell_D$) revealed that the variance of the steady-state distribution of bead position was also given by Equation 1, albeit with a renormalized ballistic length $\ell_B^{\rm eff} = v\,\tau_{\rm ON}^{\rm eff}$ (SI Appendix). With direct filament switching, the ballistic length was reduced. This is because the effective mean time $\tau_{\rm ON}^{\rm eff}$ of a run in a given direction when the beads are attached to the filaments—the *persistence* time—is reduced by direct filament switching. Note that in the absence of switching, the persistence time is simply given by the mean attachment time $1/k_{\rm off}$. The beads may also sense the net polarity of the network by switching only, i.e. without ever detaching from the filaments, and thus position themselves at the center of the antiparallel network (SI Appendix, Fig. S8). However, this mechanism would produce much steeper velocity gradients that those reported here and the diffusion profile would display a maximum at the center, in contradistinction to our observations (Fig. 4B and E; SI Appendix, Fig. S9).

Submission PDF

We studied active transport of beads coated either with myosin Va or skeletal heavy-mero myosin II. Both types of motors are double-headed molecular motors with movements directed towards the barbed ends of the actin filaments, thus away from the nucleation lines of actin polymerization (Fig. 1). However, their biophysical properties, as well as their functions in vivo, differ strongly (28). Myosin V is a processive molecular motor involved in intracellular transport (29), whereas skeletal myosin II is a non-processive motor involved in muscle contraction, not in cargo transport. Yet, both types of myosin-coated beads displayed similar transport behaviors down the net-polarity gradients of antiparallel actin networks, resulting in bead positioning (Fig. 2). Our data adds to the available evidence (30-32) that non-processive motor molecules, here myosin II, can be turned into a processive transporter if the motors work as a group on the cargo.

Positioning was more precise with beads coated with processive myosin-V than with non-processive myosin-II motors. Local analysis of bead velocity and diffusion revealed that the positioning could be described by a diffusion-drift process, for which the standard deviation of bead position is set by the ratio of an effective diffusion coefficient and an effective velocity gradient (Fig. 4). The velocity gradient was larger by a factor ~1.5 with myosin II than with myosin V. However, the effective diffusion coefficient was larger by a bigger factor (~2.2) with myosin II, resulting in less precise cargo positioning with this motor type. Our 3-state model of active bead transport reveals that the key motor property that controls positioning precision (Eq. 1) is actually the ballistic length $\ell_B = v/k_{\mathrm{OFF}}$, which is given by the ratio of the bead velocity v in an attached state to actin and the bead detachment rate k_{OFF}.

Although myosin-II and myosin-V motors have been extensively characterized at the single molecule level (28), beads are each transported by a group of motors. How multiple motor molecules coordinate or impede their movements to collectively mediate cargo motion remains unclear (11, 33). Relating the stochastic properties of bead dynamics to known properties of single motors is an avenue for future research but is beyond the scope of this work. Generally, increasing the number of motors on a bead is expected to increase the ballistic length ℓ_B (32). As already discussed above, whether or not increasing ℓ_B results in more precise positioning actually depends on how the ballistic length compares with the diffusive length ℓ_D (Fig. 5).

Our analysis of active transport indicates that bead positioning not only depends on intrinsic motor properties but also on the architecture of the actin network (Eq. 1). In particular, the lower the mean actin length λ, and thus the steeper the net-polarity gradient (Fig. 1C, inset), the sharper the positioning of the beads at the center of the antiparallel network. This condition holds true as long as the ballistic length ℓ_B remains smaller than λ to ensure centering (i.e. $\sigma < \lambda$). In addition, the precision of bead positioning can depend on the total actin density, but only at densities that are low enough that $\rho_0 \ll \rho_c = D_\phi/(\ell_B^2 k_{ON})$. In this case, the higher the actin density, the more precise the positioning. At high actin densities ($\rho_0 \gtrsim \rho_c$), positioning instead becomes independent on the total actin density, as observed in our experiments (SI Appendix, Fig. S2B). Altogether, our results emphasize the interplay between intrinsic motor properties and the architecture of the actin network for active positioning of myosin-transported cargoes.

Materials and Methods

Micro-patterning of an actin nucleation-promoting factor (pWA). Details of the micro-patterning protocol have been published elsewhere (18, 19). In short, glass coverslips were oxidized with an oxygen plasma for 3 min and incubated with 0.1 mg/ml Poly(L-lysine)-graft-poly(ethylene glycol) (PLL-g-PEG; Jenkem Technology) in 10 mM HEPES at pH = 7.4 for 30 min. The passivated surface was exposed to deep UV light (wavelength: 180 nm; UVO Cleaner Unit 342, Jelight Company INC) for 5 min through a transparent micropattern that was drawn on a chromium synthetic-quartz photomask (Toppan Photomasks). The coverslips were then incubated with 1 µM pWA in a buffer containing 50 mM KCl, 1 mM $MgCl_2$, 1 mM EGTA and 10 mM imidazole-HCl (pH = 7.8) for 10 min. In our experiments, the pattern was typically composed of seven parallel lines that were 3-µm wide, 350-µm long and spaced by 40 µm.

Actin polymerization. To induce actin polymerization from surface micro-patterns of the nucleation-promoting factor pWA, 4 µM globular actin (Tebu-Bio), 12µM profilin and 10 nM Arp2/3 complex (Tebu-Bio) were mixed in a buffer containing 10 mM imidazole-HCl (pH = 7.8), 50 mM KCl, 1 mM $MgCl_2$, 2.6 mM Na_2ATP, 56 mM dithiothreitol, 0.1 mg/ml glucose, 3.7 Units/ml catalase, 37.3 Units/ml glucose oxidase and 0.4% (w/w; macrocospic viscosity 800 cP) methylcellulose. To visualize actin filaments, 20% of the monomers were labelled with a fluorophore (Alexa568; Life Technologies). A Peltier element and feedback control (Warner Instruments) ensured that experiments were performed at a temperature of 27°C. A surface micropattern of seven parallel actin-nucleation lines resulted in six identical antiparallel networks of overlapping actin filaments.

Bead functionalization with myosins. To study cargo transport in actin networks, we added functionalized beads to the actin-polymerization solution described in the preceding section. We used polystyrene beads of 200 nm in diameter (Life Technologies). A 1-µl volume of a bead stock at 0.1% (w/w), corresponding to ~2.3×10^8 beads, was added to 24 µl of a buffer containing 80 mM KCl, 10 µM EDTA, 1 mM EGTA and 10 mM imidazole-HCl. The bead suspension had a concentration of 40 µg/ml. The beads were washed by centrifuging the solution at 20,000 g for 30 min at 4°C and by then replacing 19 µl of the supernatant with the same volume of buffer. After dispersing the beads in the solution by manual trituration followed by sonication during 30 s, we added 3 µl of a myosin solution at 0.44 µM and allowed the myosin molecules to absorb onto the surface of the beads for an incubation time of 10 min. Finally, a volume of 3 µl of BSA at 10% (w/w) was added to passivate the portion of the beads' surface that was not occupied by the myosin. The initial concentration of the myosin in the solution was 47 nM. For bead-transport studies, the concentration of functionalized beads was adjusted by dilution to ~6×10^5 μl^{-1}.

We used either of two types of myosin molecules. First, recombinant double-headed myosin Va missing the C-terminal globular tail were produced as described (34). Second, heavy-mero myosin II, purified from rabbit pectoral muscle, was kindly provided by Matthias Rief's group (TUM, Germany). In control experiments with passive beads, we omitted to add myosin and instead fully passivated the bead surface with BSA.

Microscopic observation. Our samples were viewed through a ×20 objective (NA=0.75) of a spinning-disk confocal microscope (Eclipse Ti, Nikon); this low magnification allowed us to record hundreds to thousands of bead trajectories. We recorded time-lapse videos with a CCD camera (CoolSNAp HQ2, Photometrics) at a framerate of 3 s. In the sample plane, the pixel size of the camera was 322.5 nm × 322.5 nm. Time-lapse recordings started 10 min after the injection of the polymerization mix into the flow chamber and lasted for 20 min. Note that the functionalized beads were already present in the solution used for actin polymerization at the initiation of the polymerization process. For the characterization of the actin-network florescence profiles (Fig. 1), we used a ×40 objective (NA=0.75).

Single-particle tracking. We automatically measured bead trajectories using TrackMate (35), a single-particle tracker developed as a plugin for the image-processing software Image J (National Institute of Health, Bethesda, USA). Bead tracking was performed with a time resolution of 3 s, corresponding to the framerate of our time-lapse videos. An experiment produced up to 5,000 trajectories. We filtered the data in two ways. First, we cut the portions of any trajectory for which the standard deviation of the bead position remained below 0.1 µm during at least 45 s. Some beads took several minutes to start moving after they appeared in the field of view, or showed long pauses in their trajectory before moving again, or stopped until the end of the video. Any given trajectories could thus be parsed in 2–5 tracks per trajectory during a 20-min recording. Second, we retained only the tracks that explored a region that could be inscribed in a disk with a diameter larger than 2 µm, thus rejecting shorter tracks. This procedure rejected about half of the available tracks. Tracks were typically collected from six identical lanes of the surface micropattern (see above), corresponding each to an area 350 µm × 40 µm. We assumed translational invariance of the actin network in a direction parallel to the nucleation lines as well as periodicity in the perpendicular direction (defined respectively as Y- and X-axis, see Fig. 1). These features allowed for data folding as well as spatial averaging.

In our experiments, there was a slow continuous flux of beads from the bulk to the plane of observation within the actin network. Different beads thus appeared at different times on the actin network. Any given frame of a time-lapse video in turn showed a mix of 'old' beads that were given enough time to reach steady state and of 'young' beads, mainly positioned near the nucleation lines, which were en-route towards the center of the antiparallel actin network (Fig. 2). To estimate the steady-state distribution of bead positions, we scanned all the tracks of the mobile beads to select those (~100 tracks) that lasted at least 200 s; each bead position $X(t = T_{\mathrm{EQ}})$ was then registered at time $t = T_{\mathrm{EQ}} = 200$ s after the start of its track and we computed the corresponding distribution $P_{\mathrm{M}}(X)$. The duration T_{EQ} corresponds to the travel time of a bead moving at a mean velocity 0.1 µm/s

Submission PNAS

from a nucleation line to the center of an antiparallel network if the spacing between nucleation lines is 40 µm. To allow for easy comparison of the bead trajectories along the X-axis (Fig. 2B, F and J), the time origin of each track was reset to the time were the bead first appeared on the time-lapse video.

Profiles of drift velocity and diffusion coefficient. We computed the profiles of the local drift velocity $V(X)$ and of the local diffusion coefficient $D(X)$ of the beads as a function of bead position X. To estimate $V(X)$ and $D(X)$, we measured the distribution of displacements $\Delta X_i(X)$ during a fixed time-interval τ of all the beads $i = 1, \ldots, N_X$ that are found during their trajectory at a given position X with a precision of 0.1 µm and computed the mean value $\langle \Delta X \rangle = (1/N_X) \sum_1^{N_X} \Delta X_i = V(X)\,\tau$ and its variance $\langle (\Delta X)^2 - \langle \Delta X \rangle^2 \rangle = 2D(X)\,\tau$. Knowing the profiles $V(X)$ and $D(X)$, we calculated the probability density $P_{DD}(X) = P_0 \exp\left(\int_0^X V(x)/D(x)\ \mathrm{d}x\right)$ of bead positions expected from a diffusion-drift process at steady state (see main text). In practice, we used τ = 12 s; we checked that the estimated probability density $P_{DD}(X)$ remained nearly unchanged for variations of τ in the range 3-24 s. Over a timescale τ, the beads moved on average by less than 100 nm and the net polarity of the actin network (Fig. 1C, inset) varied by less than 2%. The calculated distribution $P_{DD}(X)$ was confronted to the bead distribution $P_{\mathrm{M}}(X)$ measured directly by the procedure described in the preceding paragraph (Fig. 4C and F).

Acknowlegements:

We are indebted to M. Rief for providing the heavy-mero myosin II molecules. We acknowledge the use of microscopes from the Cell and Tissue Imaging Center (PICT-IBiSA) of the Institut Curie, which is a member of the French National Research Infrastructure France-BioImaging (ANR10-INBS-04). We thank John Manzi from the Biochemisty, Molecular Biology and Cells platform of Laboratoire Physico-Chimie Curie (Institut Curie) for protein purification and characterization. We also thank Julie Plastino and Cécile Sykes for fruitful discussions and for sharing their expertise about actin polymerization. This work was supported by the French National Agency for Research (ANR-12-BSV5 0014; awarded jointly to P.M. and L.B.), by the Labex Celtisphybio ANR-10-LABX-0038 part of the Idex PSL, by the United States National Institutes of Health R01 Grant GM097348 (awarded to E. M. D. L. C.), and by the European Research Council (741773 (AAA); awarded to L.B.). E.M.D.L.C. was a Mayent-Rothschild Senior Researcher Fellow at the Institut Curie. M.R. is alumnus of the Frontiers in Life Science PhD program of Université Paris Descartes.

Supporting Online Appendix: Figs. S1 and S2 (section 1), Supplementary Text (sections 2 to 4, with Figs. S3-S9), Table S1-S2 (section 5).

1. Howard J (2001) Mechanics of motor proteins and the cytoskeleton.
2. Blanchoin L, Boujemaa-Paterski R, Sykes C, Plastino J (2014) Actin dynamics, architecture, and mechanics in cell motility. *Physiol Rev* 94:235-263.
3. Ross J L, Ali M Y, Warshaw D M (2008) Cargo transport: molecular motors navigate a complex cytoskeleton. *Curr Opin Cell Biol* 20:41-47.
4. Lombardo A T *et al.* (2017) Myosin Va molecular motors manoeuvre liposome cargo through suspended actin filament intersections in vitro. *Nat Commun* 8:15692.
5. Leduc C, Pavin N, Jülicher F, Diez S (2010) Collective behavior of antagonistically acting kinesin-1 motors. *Phys Rev Lett* 105:128103.
6. Derivery E *et al.* (2015) Polarized endosome dynamics by spindle asymmetry during asymmetric cell division. *Nature* 528:280.
7. Kapitein L C *et al.* (2010) Mixed microtubules steer dynein-driven cargo transport into dendrites. *Curr Biol* 20:290-299.
8. Hariadi R F, Cale M, Sivaramakrishnan S (2014) Myosin lever arm directs collective motion on cellular actin network. *Proc Natl Acad Sci USA* 201315923.
9. Brawley C M, Rock R S (2009) Unconventional myosin traffic in cells reveals a selective actin cytoskeleton. *Proc Natl Acad Sci USA* 106:9685-9690.
10. Schindler T D, Chen L, Lebel P, Nakamura M, Bryant Z (2014) Engineering myosins for long-range transport on actin filaments. *Nat Nanotechnol* 9:33.
11. Sivaramakrishnan S, Spudich J A (2009) Coupled myosin VI motors facilitate unidirectional movement on an F-actin network. *J Cell Biol* 187:53-60.
12. Derr N D *et al.* (2012) Tug-of-war in motor protein ensembles revealed with a programmable DNA origami scaffold. *Science* 338:662-665.
13. Guérin T, Prost J, Martin P, Joanny J-F (2010) Coordination and collective properties of molecular motors: theory. *Curr Opin Cell Biol* 22:14-20.
14. Klumpp S, Lipowsky R (2005) Cooperative cargo transport by several molecular motors. *Proc Natl Acad Sci USA* 102:17284-17289.
15. Erdmann T, Schwarz U S (2012) Stochastic force generation by small ensembles of myosin II motors. *Phys Rev Lett* 108:188101.
16. Kolomeisky A B (2013) Motor proteins and molecular motors: how to operate machines at the nanoscale. *J Phys Condens Matter* 25:463101.
17. Jülicher F, Ajdari A, Prost J (1997) Modeling molecular motors. *Rev Mod Phys* 69:1269.
18. Reymann A C *et al.* (2010) Nucleation geometry governs ordered actin networks structures. *Nat Mater* 9:827-832.
19. Reymann A C, Guerin C, Thery M, Blanchoin L, Boujemaa-Paterski R (2014) Geometrical control of actin assembly and contractility. *Methods Cell Biol* 120:19-38.
20. Letort G *et al.* (2015) Geometrical and mechanical properties control actin filament organization. *PLoS Comput Biol* 11:e1004245.
21. Pfeffer S R (1999) Transport-vesicle targeting: tethers before SNAREs. *Nat Cell Biol* 1:E17.
22. Lipowsky R, Klumpp S, Nieuwenhuizen T M (2001) Random walks of cytoskeletal motors in open and closed compartments. *Phys Rev Lett* 87:108101.
23. Müller M J, Klumpp S, Lipowsky R (2005) Molecular motor traffic in a half-open tube. *J Phys Condens Matter* 17:S3839.
24. Naoz M, Manor U, Sakaguchi H, Kachar B, Gov N S (2008) Protein localization by actin treadmilling and molecular motors regulates stereocilia shape and treadmilling rate. *Biophys J* 95:5706-5718.
25. Zhuravlev P I, Lan Y, Minakova M S, Papoian G A (2012) Theory of active transport in filopodia and stereocilia. *Proc Natl Acad Sci USA* 109:10849-10854.
26. Hancock W O (2014) Bidirectional cargo transport: moving beyond tug of war. *Nat Rev Mol Cell Biol* 15:615.
27. Müller M J, Klumpp S, Lipowsky R (2008) Tug-of-war as a cooperative mechanism for bidirectional cargo transport by molecular motors. *Proceedings of the National Academy of Sciences* 105:4609-4614.
28. De La Cruz E M, Ostap E M (2004) Relating biochemistry and function in the myosin superfamily. *Curr Opin Cell Biol* 16:61-67.
29. Hammer III J A, Sellers J R (2012) Walking to work: roles for class V myosins as cargo transporters. *Nat Rev Mol Cell Biol* 13:13.
30. Kachar B (1990) Polarity and velocity of sliding filaments: control of direction by actin and of speed by myosin. *Science* 249:406-408.
31. Nagy A *et al.* (2012) Kinetic characterization of nonmuscle myosin IIb at the single molecule level. *J Biol Chem* jbc. M112. 424671.
32. West J M, Higuchi H, Ishijima A, Yanagida T (1996) Modification of the bi-directional sliding movement of actin filaments along native thick filaments isolated from a clam. *J Muscle Res Cell Motil* 17:637-646.
33. Ali M Y, Vilfan A, Trybus K M, Warshaw D M (2016) Cargo transport by two coupled myosin Va motors on actin filaments and bundles. *Biophys J* 111:2228-2240.
34. Olivares A O, Chang W, Mooseker M S, Hackney D D, Enrique M (2006) The tail domain of myosin Va modulates actin binding to one head. *J Biol Chem* 281:31326-31336.
35. Tinevez J Y *et al.* (2017) TrackMate: An open and extensible platform for single-particle tracking. *Methods* 115:80-90.

Submission PDF